# Automated Design of a Three-Dimensional Subsonic Diffuser

Wei-Li Zhang,* Doyle D. Knight,† and Don Smith‡
*Rutgers University, New Brunswick, New Jersey 08903*

**A novel methodology is developed to integrate state-of-the-art computational fluid dynamics analysis, NURBS, and optimization theory to reduce total pressure distortion and sustain total pressure recovery within a curved three-dimensional subsonic S-duct diffuser by automated redesign of the diffuser shape. Two independent design variables are used. The change of the surface shape is assumed to be Gaussian. GASP with the modified Baldwin–Lomax turbulence model (Baldwin, B. S., and Lomax, H., "Thin Layer Approximation and Algebraic Model for Separated Turbulent Flows," AIAA Paper 78-257, 1978) is employed for the flowfield prediction and proved to give good agreement with the experimental surface pressure for the baseline S-duct diffuser geometry. The automated design optimization is performed with a gradient-based method to minimize the total pressure distortion based on the two design variables. The best configuration obtained reduced distortion by typically 70% while keeping the total recovery essentially the same. The results indicate that the mechanism responsible for improved diffuser performance is the suppression of detrimental secondary flows by changing the surface shape to redirect the flow.**

## Nomenclature

$C_p$ = pressure coefficient
$DC(\phi)$ = distortion index
$d$ = inflow diameter
$H$ = inflow boundary-layer shape factor
$n$ = distance normal to surface
$p$ = static pressure
$p_0$ = total pressure
$q$ = dynamic pressure
$R$ = radius of curvature of baseline duct
$r_1$ = inlet radius of baseline duct, 10.21 cm
$r_2$ = outlet radius of baseline duct, 12.57 cm
$s$ = arclength measured along duct centerline
$s_0$ = centroid of perturbation to control points
$u_*$ = friction velocity
$\alpha$ = magnitude of perturbation to control points
$\beta$ = width of pertubation to control points
$\delta$ = inflow boundary-layer thickness
$\delta_1$ = inflow displacement thickness
$\delta_2$ = inflow momentum thickness
$\theta$ = angle measured along duct
$\phi$ = angular width of region for $DC$

*Subscript*

cl = centerline

## Introduction

**A**IRCRAFT propulsion systems often use diffusers to convey airflow from the wing or fuselage intake to the engine compressor. Compressible, subsonic flow conditions usually exist for this application. Examples of commercial aircraft with such diffusers include the Boeing 727 and the Lockheed Tristar. Among military aircraft, both the General Dynamic F-16 and McDonnell-Douglas F-18 use them.

Well-designed diffusers should incur minimal total pressure losses and deliver nearly uniform flow with small transverse velocity components at the engine compressor entrance. Reduced total pressure recovery lowers propulsion efficiency, whereas nonuniform flow conditions at the engine face lower engine surge and stall limits. However, airframe weight and space considerations demand as short a diffuser as possible, resulting in high degrees of centerline curvature and large changes in cross-sectional area. These factors are responsible for the development of strong secondary flow and attendant boundary-layer separation, which increase the total pressure nonuniformity and total pressure loss at the diffuser exit. Large amounts of distortion significantly reduce engine performance and may lead to drastic results, such as engine stall.

The flowfield characteristics and performance of subsonic diffusers has been an interesting research topic for many years. A very early experimental investigation was performed by Weske.[1] He performed a systematic investigation of the pressure drop and, in some cases, of the velocity distribution in compound elbows to improve the design of ducting systems in aircraft. In his research, circular and elliptical ducts were configured with different angular positions relative to each other. He demonstrated that the radius ratio (defined as the ratio of the radius of curvature of the centerline of the duct to the hydraulic diameter of the duct) is the most important design variable for the compound bends affecting the pressure-drop coefficient of the bend, although the variation of the centerline of the compound bend also contributes to the pressure drop. Flow rotation was discovered downstream of a 90-deg-offset compound bend. Henry[2] summarized a correlation of previous experimental data on duct components of aircraft power-plant installations and stated that skin friction and flow separation are two fundamental causes of pressure loss in fully turbulent flow through any duct component. He also indicated that pressure loss in the flow is mainly due to flow separation and that forces arising in the airstream in a direction opposite to the direction of flow and the change of flow direction, as in bends, tends to cause flow separation.

Bansod and Bradshaw[3] investigated the total pressure, static pressure, surface shear stress, and yaw angle in the flow through several S-shaped ducts, each with a thin turbulent boundary layer at entry. They found that the large extent of the low-velocity region at the exit plane is due to the production of longitudinal vorticity by lateral deflection of the boundary-layer flow in the first bend, followed by vortex stretching caused by a region of longitudinal acceleration (for the particular diffusers studied) toward the end of the second bend. A pair of contrarotating vortices was also found embedded in the lower part on the exit and expelled low-velocity fluid toward the center of the cross section. The same mechanism appears to be responsible for the region of low total pressure region. Guo and Seddon[4] also reached a similar conclusion in their experiment to measure the static pressure, total pressure, swirl, and three-dimensional

turbulence in the flow through an S-shaped rectangular duct at different incidences, yaw angles, and mass flow ratios. Their results also showed, at high incidence, the distortion of total pressure at the exit of the S-duct is large and indicated that appreciation of the existence of this type of flow is important in the field of air intake design for jet aircraft.

Wellborn et al.[5] provided a comprehensive experimental benchmark data set for compressible flow through a representative subsonic diffuser and investigated the details of the flow separation region and the mechanisms that drive this complicated flow phenomenon. This diffuser is the baseline configuration for our design optimization and is described in detail in the next section. This research described the flow through an S-duct that is characterized by a strong interaction between the boundary layer and the core flow. It also showed that the flow was symmetric about the $y = 0$ plane. A large region of flow separation was found within the duct. Duct curvature induced strong pressure-driven secondary flows that evolved into a large pair of counter-rotating vortices. These vortices convected the low-momentum fluid of the boundary layer toward the center of the duct, degrading both the uniformity and magnitude of the total pressure profile.

Abdallah and Hamed[6] performed an inviscid computation for the secondary flow in curved ducts by presenting an analytical formulation and a numerical solution for three-dimensional rotational flow in curved ducts to study the secondary flow phenomenon associated with the distributed secondary vorticity. Smith et al.[7] performed computational fluid dynamic (CFD) studies by using a parabolized Navier–Stokes (PNS) program, PARC3D, to predict the complex flow physics and performance characteristics of a diffusing subsonic S-duct. An algebraic turbulence model, together with the Beam and Warming approximate factorization algorithm, was used to solve the three-dimensional Reynolds-averaged Navier–Stokes equations. This computation demonstrated good agreement with the experimental data, and it also suggested that upstream and downstream boundary conditions for the duct should be accurately specified to allow for the proper upstream boundary-layer development and downstream pressure adjustment. Harloff et al.[8,9] performed Navier–Stokes analysis and experimental data comparison of compressible flow within a circular diffusing S-duct and a circular-to-rectangular transition duct with a full Navier–Stokes solver, PARC3D, using both an algebraic and a two equation turbulence model. This computation indicated that the flowfields were generally in good agreement with the experiment; however, both turbulence models underpredicted the length and angular extent of the boundary-layer separation.

Another method of predicting the properties of various turbulence flows in planar, conical, and annular diffusers with inlet swirl and inlet distortion effect was developed and appraised by Hah,[10] Harloff et al.,[11] and Demuren,[12] and the feasibility of conducting three-dimensional Navier–Stokes calculations for circular-to-rectangular transition ducts was performed by Pao et al.[13]

Because engine face flow distortion is one of the most troublesome problems for aircraft designers of modern inlet engine systems, a large effort has been made to improve the diffuser performance by redesigning the diffusers to reduce the distortion at the engine face. Gerlach and Schroeder[14] performed a theoretical and experimental investigation of ducts and their components to minimize pressure drop, surge pressures, and vibration levels to generally improve flow conditions of gases and liquids in space vehicle feed systems. By changing the duct cross-sectional shape, local accelerations and decelerations of fluid were achieved to reduce the overall elbow pressure loss and centrifugal force gradient. Some researchers tried to reduce the flow separation and secondary flow in different ways. Guo and Seddon[4] tried to reverse the sense of the swirl at the exit plane by implementing a solid spoiler to block 15% of the entry width from the inside wall. Weng and Guo[15] presented an automatic adjustable blade method to control the swirl and to improve the average total pressure coefficient in an S-duct. A airfoil vortex device and flow control rail were used to reduce the swirl by Vakili et al.[16] Lin and Jules[17] described a vortex control device that decreased the swirl with increasing suc-

tion and even eliminated the bulk vortex if the suction was large enough.

Another important way to reduce or eliminate boundary-layer separation is related to vortex generators. Substantial improvements in pressure recovery were reported by Taylor[18] and Brown et al.[19] on various subsonic diffuser geometries. Work done at NASA John H. Glenn Research Center at Lewis Field on a mixed-compression inlet by Mitchell and Davis[20] established the principle of using vortex generator arrays as a means of reducing exit airflow distortion. Reichert and Wendt[21] performed experimental research by installing vortex generator in the diffuser to reduce the distortion. In their experiment, different kinds of vortex generators were intensively investigated with different configurations. Anderson and Gibb[22] demonstrated that a reduced Navier–Stokes solver can be used very effectively to develop a vortex generator installation to minimize the engine face circumferential distortion by controlling secondary flow. This research study also established the nature of the performance improvements that can be realized with vortex flow control and suggested a set of aerodynamic properties that can be used to achieve a successful vortex generator installation design. Vakili et al.[16] showed that an array of vane-type vortex generators reduced total pressure distortion at the duct exit. Most recently, Mayer[23] designed a three-dimensional subsonic diffuser by changing the diffuser shape with the aid of CAD software. After defining the throat and engine face cross sections, the aerodynamic surfaces of the diffuser were formed using smooth surface blends from the throat section to the engine face with the constraint of line-of-sight blockage of the engine face. The results showed that the shape of the diffuser is closely related to the distortion, and the resulting diffuser is capable of reducing the distortion while maintaining acceptable total pressure recovery and preserving line-of-sight blockage. Shape optimization and the relation between the components in the propulsion were also extensively studied by Reddy and Reddy,[24] Burgreen et al.,[25] and Lin and Jules.[17]

With the advent of high-speed computers and the availability of more accurate and reliable CFD solvers, numerical optimization processes can be effectively used to carry out complex shape design for optimum performance. Compared to the traditional methods, this process involves modest cost and can be completed in a short period of time. The objective of the present research is to develop a methodology to integrate a state-of-art surface representation technique, structured grid generation, a viscous Reynolds-averaged Navier–Stokes solver, and sequential quadratic optimization theory to minimize the total pressure distortion at the exit plane of a three-dimensional subsonic diffuser while maintaining or increasing the total pressure recovery on that plane by modifying the shape of the S-shaped diffuser.

## Baseline Diffuser

The baseline diffuser corresponds to the experimental configuration of Wellborn et al.[5] The geometry is shown in Fig. 1. The duct centerline was defined by two planar circular arcs with identical radii $R$, of 102.1 cm, and subtended angles $\Theta_{max}/2$, of 30 deg. The centerline coordinates are given by Eqs. (1) and (2). All cross sections perpendicular to the centerline were circular. The duct inlet radius $r_1$ was 10.21 cm. The duct exit radius $r_2$ was 12.57 cm and produced an area ratio $A_2/A_1$ of 1.52. The variation of the duct radius as a function of the angle $\theta$ is given by Eq. (3). The data of this experiment, performed at the NASA John H. Glenn Research Center at Lewis Field Internal Flow Mechanics Facility, are presented by Wellborn et al.[5] Complete details of the facility are described by Porro et al.[26] For $0 \leq \theta \leq \theta_{max}/2$

$$x_{cl} = R \sin\theta, \qquad y_{cl} = 0, \qquad z_{cl} = R \cos\theta - R \quad (1)$$

For $\theta_{max}/2 \leq \theta \leq \theta_{max}$

$$x_{cl} = 2R \sin(\theta_{max}/2) - R \sin(\theta_{max} - \theta), \qquad y_{cl} = 0$$

$$z_{cl} = 2R \cos(\theta_{max}/2) - R - R \cos(\theta_{max} - \theta) \quad (2)$$

$$r/r_1 = 1 + 3(r_2/r_1 - 1)(\theta/\theta_{max})^2 - 2(r_2/r_1 - 1)(\theta/\theta_{max})^3 \quad (3)$$

**Table 1  Inlet boundary-layer parameters**

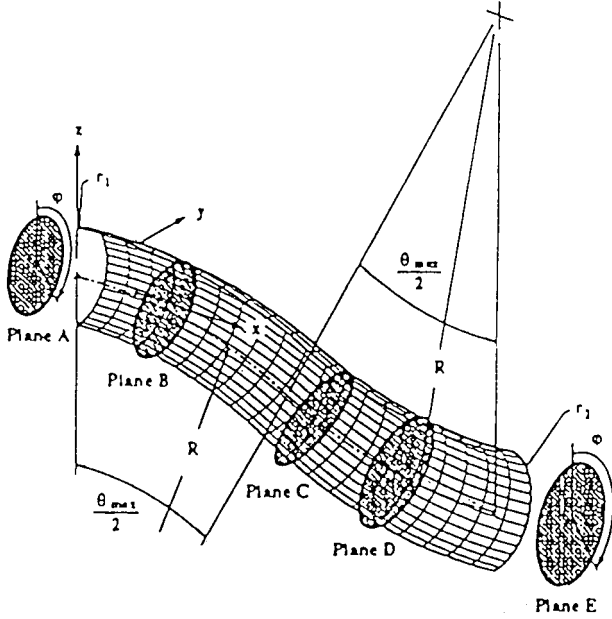| Profile parameter | Value |
|---|---|
| $(\delta/r_1) \times 100$ | 6.95 |
| $(\delta_1/r_1) \times 100$ | 1.46 |
| $(\delta_2/r_1) \times 100$ | 1.06 |
| $H$ | 1.38 |



**Fig. 1  Baseline S-duct diffuser.**

All reported tests were conducted with an inlet centerline Mach number of 0.6 and an axisymmetric inflow. The Reynolds number, based on the inlet diameter and centerline velocity, was $2.6 \times 10^6$. An axisymmetric thin turbulent inlet boundary layer existed. The inlet profile parameters are shown in Table 1.

## Governing Equations

The integral form of the time-dependent compressible Reynolds-averaged Navier–Stokes equations in three dimensions is

$$\frac{\partial}{\partial t} \int_V Q \, dV + \oint_A [F(Q) \cdot \hat{n}] \, dA = \oint_A [F_v(Q) \cdot \hat{n}] \, dA \quad (4)$$

The conserved quantities are denoted by $Q$, the inviscid flux vector by $F$, and viscous flux vector by $F_v$. The normal direction vector of the surface is denoted by $\hat{n}$. Every cell in the domain is used as a control volume for application of Eq. (4). If we denote the cell volume as Vol and the area of each cell face as $\Delta A$, then the finite volume form of Eq. (4) is

$$\text{Vol} \left( \frac{\partial \bar{Q}}{\partial q} \right) \frac{\partial q}{\partial t} + \sum_A (F \cdot \hat{n}) \Delta A = \sum_A (F_v \cdot \hat{n}) \Delta A \quad (5)$$

where the cell average of the conserved-variable field is defined as

$$\bar{Q} \equiv \frac{1}{\text{Vol}} \int_V Q \, dV \quad (6)$$

In vector form, the conservative and primitive variables are

$$Q = \begin{Bmatrix} \rho \\ \rho u \\ \rho v \\ \rho w \\ \rho e \end{Bmatrix}, \qquad q = \begin{Bmatrix} \rho \\ u \\ v \\ w \\ p \end{Bmatrix} \quad (7)$$

The flux vectors represent, in order, the species continuity equation, the three momentum equations, and the energy equation. The inviscid flux vector is

$$F \cdot \hat{n} = \begin{Bmatrix} \rho(V \cdot \hat{n}) \\ \rho u(V \cdot \hat{n}) + \hat{n}_x p \\ \rho v(V \cdot \hat{n}) + \hat{n}_y p \\ \rho w(V \cdot \hat{n}) + \hat{n}_z p \\ \rho h(V \cdot \hat{n}) \end{Bmatrix} \quad (8)$$

and the viscous flux vector is

$$F_v \cdot \hat{n} = \begin{Bmatrix} 0 \\ \tau \cdot \hat{n} \\ -(\nabla q + \tau V) \cdot \hat{n} \end{Bmatrix} \quad (9)$$

where $V$ is the velocity vector and $\tau$ is the viscous-stress tensor. Details are presented by Zhang.[27] The heat conduction vector is

$$\nabla q \equiv -\hat{k} \nabla T \quad (10)$$

where $\hat{k}$ is molecular thermal conductivity. Sutherland's relation is used and is written as follows:

$$\hat{k} = \hat{k}_0 (T/T_0)^{\frac{3}{2}} [(T_0 + S)/(T + S)] \quad (11)$$

The coefficients $\hat{k}_0$, $T_0$, and $S$ depend on the species. More details may be found by White.[28] The Baldwin–Lomax algebraic turbulence model[29] is used. The search for the peak in the outer function $n\omega D$ (where $n$ is the distance normal to the wall, $\omega$ is the modulus of the vorticity, and $D$ is the VanDriest damping factor) is restricted to a distance of $\delta$ from the wall, where $\delta$ is the incoming boundary-layerthickness.[9,30] This avoids a spurious definition of the outer length scale. Details are presented by Zhang.[27] The Reynolds-averaged Navier–Stokes equations are solved in finite volume form using general aerodynamic simulation program (GASP).[31] The inflow boundary condition is a nonseparated turbulent flow, and it plays an important role in the flow separation and secondary flow in the downstream part of the diffuser. It is essential to supply an accurate inflow to simulate the complicated flowfield within the diffuser. A two-dimensional, compressible turbulent boundary-layer flow solver developed by York[32] was used to compute the inflow profile. The pointwise inflow boundary condition was constructed based on the method of characteristics. At the outflow boundary, the back pressure is held constant over the entire boundary surface, and the remaining flow variables are set equal to those on the first interior cells. The value of the back pressure is obtained from experiment. Provided that the outflow is located at the end of a section of straight, constant cross-sectional duct sufficiently far downstream of the region of duct centerline curvature, the assumption of constant outflow pressure is reasonable for simulation of steady flow. Typically, the outflow boundary was several diameters downstream of the end of the duct centerline curvature. No-slip and adiabatic boundary conditions are applied on the solid wall boundary.

## Algorithms

### Surface Geometry Representation

The geometry of the three-dimensional diffuser is represented by non-uniform rational B-splines (NURBS). A NURBS surface of degree $p$ in the $u$ direction and degree $q$ in the $v$ direction is in the form

$$S(u, v) = \left[ \frac{\sum_{i=0}^{n} \sum_{j=0}^{m} N_{i,p}(u) N_{j,q}(v) \omega_{i,j} P_{i,j}}{\sum_{i=0}^{n} \sum_{j=0}^{m} N_{i,p}(u) N_{j,q}(v) \omega_{i,j}} \right]$$

$$0 \leq u, v \leq 1 \quad (12)$$

The $P_{i,j}$ form a bidirectional control net. The $\omega_{i,j}$ are the weights, and $N_{i,p}(u)$ and $N_{j,q}(v)$ are the nonrational B-spline basis function defined on the knot vectors:

$$U = \left\{ \underbrace{0, \ldots, 0}_{p+1}, u_{p+1}, \ldots, u_{r-p-1}, \underbrace{1, \ldots, 1}_{p+1} \right\}$$

$$V = \left\{ \underbrace{0, \ldots, 0}_{q+1}, v_{q+1}, \ldots, v_{s-q-1}, \underbrace{1, \ldots, 1}_{q+1} \right\} \quad (13)$$

where $r = n + p + 1$, $s = m + q + 1$, and

$$N_{i,0}(u) = \begin{cases} 1 & \text{if} \quad u_i \le u < u_{i+1} \\ 0 & \text{otherwise} \end{cases}$$

$$N_{i,p} = \frac{u - u_i}{u_{i+p} - u_i} N_{i,p-1}(u) + \frac{u_{i+p+1} - u}{u_{i+p+1} - u_{i+1}} N_{i+1,p-1}(u) \quad (14)$$

A NURBS bivariate vector-valued piecewise rational function is used to define the diffuser shape. To retain the second-order continuity of the surface to be built, three degrees in both parameter $u$ and $v$ direction are chosen in the representation. We assume, without loss of generality, that $u$ is along the circumference on the cross section normal to the centerline, whereas $v$ is along the centerline. The NURBS surface is represented as

$$S(u, v) = \sum_{i=0}^{14} \sum_{j=0}^{136} R_{i,j} P_{i,j} \quad (15)$$

where

$$R_{i,j} = \left[ \frac{N_{i,3}(u) N_{j,3}(v) \omega_{i,j}}{\sum_{k=0}^{14} \sum_{l=0}^{136} N_{k,3}(u) N_{l,3}(v) \omega_{k,l}} \right] \quad (16)$$

$\{P_{i,j}\}$ form a bidimensional control net with $14 \times 136$ in $u$ and $v$ directions, respectively, and $\{\omega_{i,j}\}$ are weights set to 1.0 in the computation.

$\{N_{i,3}(u)\}$ and $\{N_{j,3}(v)\}$ are the nonrational B-spline basis functions defined on the knot vectors,

$$U = \{u_0, u_1, \ldots, u_{14}\}, \qquad V = \{v_0, v_1, \ldots, v_{136}\} \quad (17)$$

Because in the $u$ direction, the surface is closed, $P_{12,j} = P_{1,j}$, $P_{13,j} = P_{2,j}$, $P_{14,j} = P_{3,j}$.

## Flowfield Analysis

A three-dimensional, multiblock structured grid is generated by GridPro/az3000 (Ref. 33). GridPro is a general purpose commerical grid generator using an advanced smoothing scheme that incorporates many automatic features. The process of grid generation is accomplished by solving a variationally based method with an iterative updating scheme. The grid used for the results presented herein consists of an H grid of $17 \times 25 \times 265$ and O grid of $57 \times 145 \times 265$. The distance of the first grid point adjacent to the walls is restricted according to $n^+ \le 1$, where $n^+ = n u_*/\nu_w$, and $n$ is the normal distance, $u_* = \sqrt{(\tau_w/\rho_w)}$, and $\nu_w = \mu_w/\rho_w$.

To evaluate the integral in Eq. (4), the primitive variables at the cell faces are employed to evaluate the fluxes. The monotonic upstream-centered scheme for conservation laws is employed to compute the left state at the $i + \frac{1}{2}$ face and right state at the $i - \frac{1}{2}$ face:

$$q_{i+\frac{1}{2}}^l = q_i + (\phi/4)[(1-k)\nabla q_i + (1+k)\Delta q_i] \quad (18)$$

$$q_{i+\frac{1}{2}}^r = q_i - (\phi/4)[(1+k)\nabla q_i + (1-k)\Delta q_i] \quad (19)$$

where

$$\nabla q_i = q_{i+1} - q_i, \qquad \Delta q_i = q_i - q_{i-1} \quad (20)$$

In Eqs. (18) and (19), the value for $k$ determines the spatial accuracy of the reconstruction, and $\phi$ is either 0 for first-order accuracy or 1 for higher-order accuracy. The values $k = \frac{1}{3}$ and $\phi = 1$ are employed to achieve third-order quadratic reconstruction that conserves the cell average of all three cells: $q_{i-1}$, $q_i$, and $q_{i+1}$. The Van Leer et al.[34] scheme is used to compute the inviscid fluxes. To speed up computational convergence, local time stepping and a multigrid strategy are employed.

### Sequential Quadratic Optimization Method

The general constrained optimization problem is to minimize a nonlinear function subject to nonlinear constraints. The formation can be described as follows:

$$\min\{f(x): c_i(x) \le 0, i \in I, h_i(x) = 0, i \in \xi\} \quad (21)$$

where $c_i$ and $h_i$ are the mapping from $R^n$ to $R$ and $I$ and $\xi$ are index sets for inequality and equality constraints, respectively. The sequential quadratic programming algorithm CFSQP[35] is a generalization of Newton's method that minimizes a quadratic model of the problem. In this case, for each iteration $k$, the sequential quadratic programming algorithm replaces the objective function with quadratic approximation,

$$f_k(d) = f(x_k) + \nabla f(x_k)^T d + \tfrac{1}{2} d^T \nabla^2 f(x_k, \lambda_k) d \quad (22)$$

where $\{\lambda_k\}$ is the Lagrange multiplier. If the initial guess is infeasible for linear constraints, a point satisfying these constraints is generated by solving a strictly convex quadratic program, and if the initial guess, or the newly generated initial guess, is infeasible for the nonlinear inequality constraints, a point is generated to satisfy all of the constraints other than nonlinear equality constraints by iterating on the problem of minimizing the maximum of the nonlinear inequality constraints. Then according to Mayne and Polak's scheme,[36] nonlinear equality constraints are turned into inequality constraints,

$$h_j(x) \le 0, \qquad j = 1, \ldots, n_e \quad (23)$$

and the original objective function $f(x)$ is replaced by the modified objective function,

$$f_m(x, p) = f(x) - \sum_{j=1}^{n_e} p_j h_j(x) \quad (24)$$

where $p_j$, $j = 1, \ldots, n_e$ are positive penalty parameters that are iteratively adjusted. The resulting optimization problem, therefore, involves only linear constraints and nonlinear inequality constraints. The successive iterations generated all satisfy these constraints. The algorithm for this transformation is described and analyzed by Panier and Tits,[37] Bonnans and Panier,[38] and Zhou and Tits.[39] An Armijo-type line search[35] is used when minimizing the maximum of the nonlinear inequality constraints to generate an initial feasible point.

After approximation to the quadratic form by Eq. (22) on a feasible iterate $x$, the basic sequential quadratic direction $d^0$ is first computed by solving a standard quadratic program using a positive definite estimate of the Hessian matrix. An essentially arbitrary feasible descent direction

$$d^1 = d^1(x) \quad (25)$$

is then computed by solving the strictly convex quadratic program. For a certain scalar $\rho \in [0, 1]$, a feasible descent direction

$$d = (1 - \rho)d^0 + \rho d^1 \quad (26)$$

is obtained, asymptotically close to $d^0$. Then a second-order correction

$$\tilde{d} = \tilde{d}(x, d, H) \qquad (27)$$

is computed involving auxiliary function evaluations at $x + d$. $H$ is the Hessian matrix. An Armijo-type search is performed along the arc $x + td + t^2\tilde{d}$. The purpose of $\tilde{d}$ is to allow a full step to be taken to a solution, thus, allowing superlinear convergence to take place.

Automatic optimization of a three-dimensional subsonic diffuser can be realized by integrating the CFD solver GASP, grid generation GridPro, surface representation NURBS representation, and optimizer CFSQP. The Perl shell language is employed to integrate this process, to realize the communication between these major components, and to monitor the progress of the design in the process.

## Baseline Computation

Before the optimization, computations of the baseline configuration (Fig. 1) were performed to verify the accuracy of the numerical algorithm of the CFD solver GASP and the geometry surface configuration. At the inflow, the inlet Mach number at the centerline is 0.6, the inlet Reynolds number based on inlet diameter is $2.6 \times 10^6$, and the inlet boundary thickness is 7% of the inlet diameter.

A grid refinement study was performed to ascertain the grid resolution required for the optimization. For the same baseline configuration, three sets of grid were used: a coarse grid of $9 \times 9 \times 85$ of H grid and $25 \times 39 \times 85$ of O grid (149,160 grid points), a medium grid of $9 \times 13 \times 133$ of H grid and $29 \times 73 \times 133$ of O grid (297,122 grid points), and a fine grid of $17 \times 25 \times 265$ of H grid and $57 \times 145 \times 265$ of O grid (2,302,850 grid points). The first point off the wall has an average $n^+$ of less than 1.0 for all three sets. Based on this grid refinement study,[40] an effectively grid-independent solution is achieved by the refined grid. All results presented here are for the refined grid. Because the geometry and flow are symmetric about the $y = 0$ plane, we compute the flowfield in one-half of the diffuser with a symmetry boundary condition. The grid sizes given correspond to the half-domain.

The computed results for the baseline geometry are shown in Figs. 2–7 and show the static pressure coefficient $C_p$ at three circumferential locations ($\phi = 10$, 90, and 170 deg) and three streamwise stations (B, C, and D) together with the experimental data and the computation of Harloff et al.[8] The locations of the measurements are indicated in Fig. 1. The static pressure coefficient $C_p$ is defined as

$$C_p = \frac{p - p_{cl}}{p_{0,cl} - p_{cl}} \qquad (28)$$
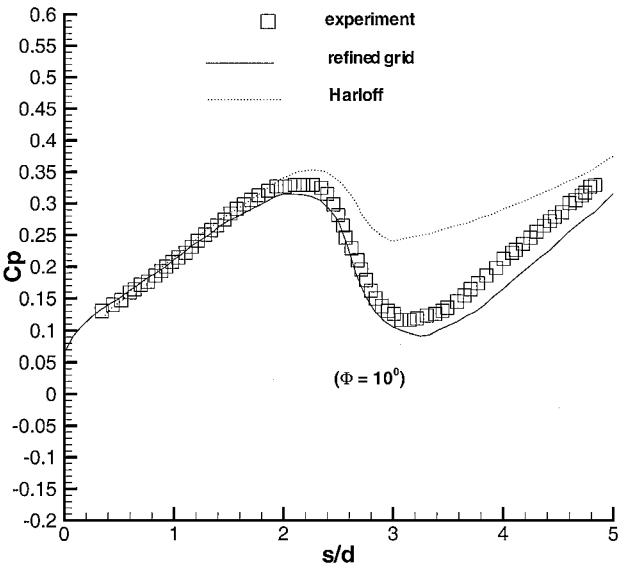


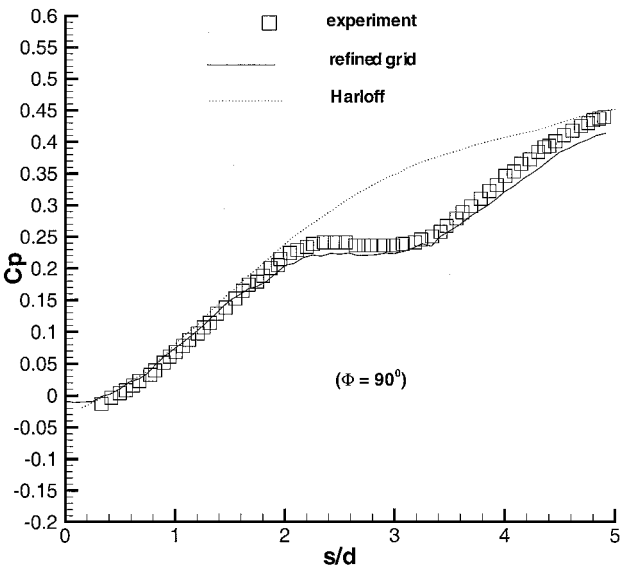Fig. 3 Surface static pressure coefficient at $\Phi = 90°$.



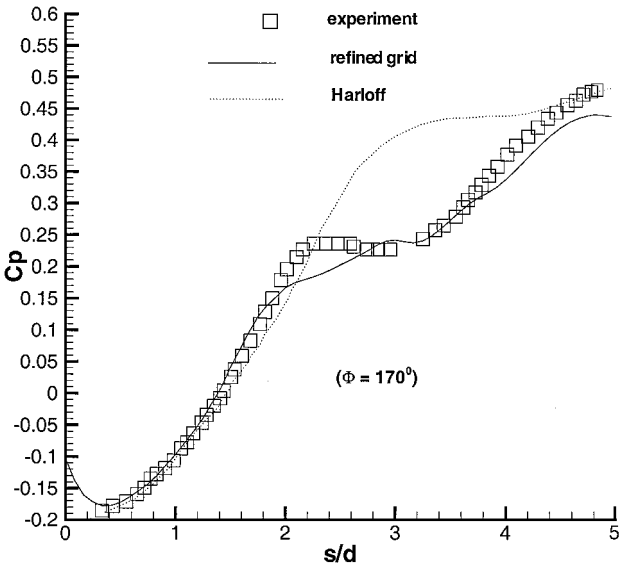Fig. 4 Surface static pressure coefficient at $\Phi = 170°$.



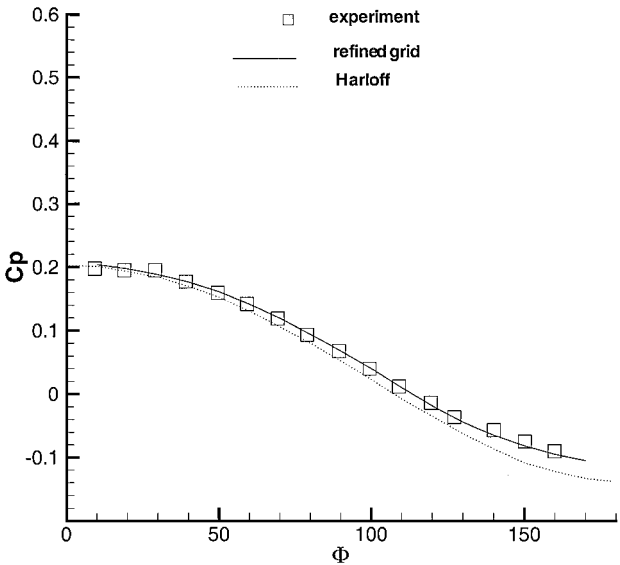Fig. 2 Surface static pressure coefficient at $\Phi = 10°$.



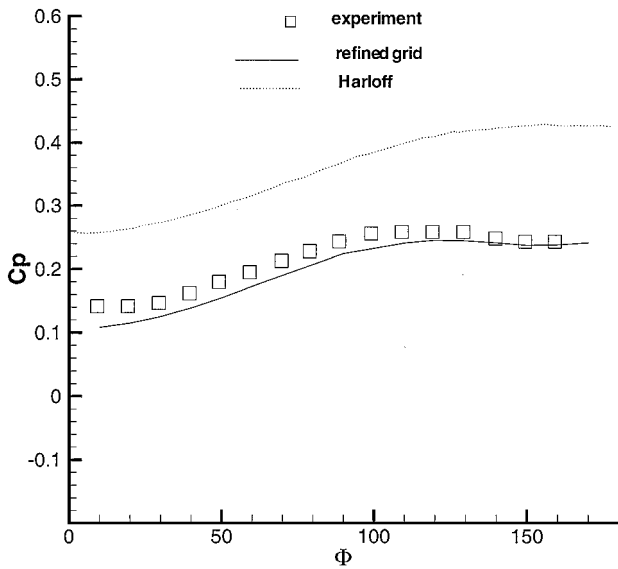Fig. 5 Circumferential surface static pressure at plane B.

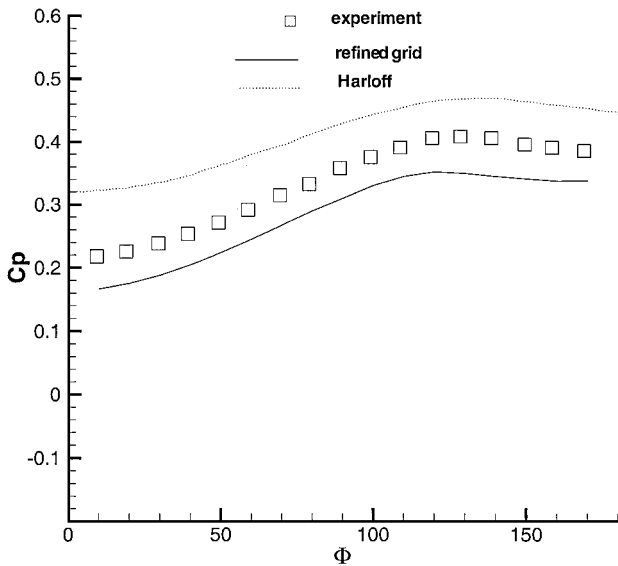Fig. 6   Circumferential surface static pressure at plane C.



Fig. 7   Circumferential surface static pressure at plane D.

where $p$ is the local static pressure, and $p_{0,cl}$ and $p_{cl}$ are the total and static pressure at the inflow centerline, respectively. Overall, the present computations display very good agreement with experiment and demonstrate a significant improvement over the previous computation of Harloff et al. The streamwise pressure distributions (Figs. 2–4) display a plateau beginning at $s/d = 1.98$, which is associated with the separation of the boundary layer on the lower surface. The crosstream pressure distribution at location B (Fig. 5) shows a circumferential pressure gradient that is attributable to the streamwise curvature of the diffuser and responsible for the generation of circumferential flow. The sign of the circumferential pressure gradient changes at location C due to the change in curvature of the diffuser and becomes larger at location D.

The experimental and computed surface streamlines for the baseline geometry are shown in Figs. 8 and 9, respectively. Reasonable agreement is observed. The computed surface streamlines display a closed limiting oval streamline and a nodal point of separation.[41] The streamwise location $s$ of the computed and experimental separation point on the centerline are shown in Table 2 and are in close agreement.

Figure 10 shows the computed and experimental total pressure coefficient contours at plane E. The experimental data are on the left. The total pressure coefficient is defined by

Table 2   Separation starting point location

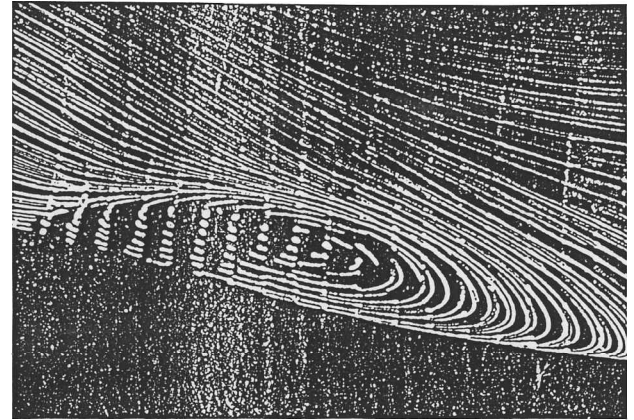| Case | Starting point location, cm |
|---|---|
| Experiment | 40.48 |
| Refined grid | 38.60 |



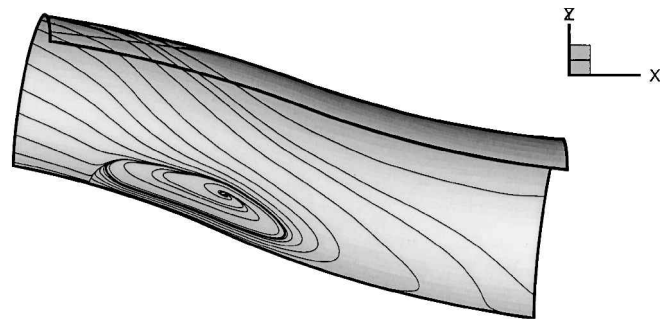Fig. 8   Experimental surface streamlines.



Fig. 9   Computed surface streamlines.

$$C_{p_0} = \frac{p_0 - p_{cl}}{p_{0,cl} - p_{cl}} \qquad (29)$$

A region of low total pressure is evident near the lower surface. It is attributable to the interaction of the strong secondary flows, initially generated by the circumferential pressure gradient (Fig. 5), with the separation of the boundary layer near the lower surface. The low-pressure region comprises a counter-rotating vortex pair. The computed shape of the low total pressure region is in reasonable agreement with experiment; however, the magnitude of the total pressure loss is overpredicted. The computed total pressure distortion indices are defined by

$$DC(\phi) = \max[\bar{p}_0 - \bar{p}_0(\phi)]/\bar{q} \qquad (30)$$

where

$$\bar{p}_0 = \frac{\int_A p_0 \, dA}{\int_A \, dA}, \qquad \bar{p}_0(\phi) = \frac{\int_\phi p_0 \, dA}{\int_\phi \, dA}, \qquad \bar{q} = \frac{\int_A q \, dA}{\int_A \, dA} \qquad (31)$$

and $\int_\phi$ indicates an integration over a pie-shape domain of angular size $\phi$ (Fig. 10), and $\int_A$ indicates an integration over the entire cross-sectional area $A$. The maximum is taken over all possible locations of the pie-shaped domain. The distortion indices are defined at plane E (Fig. 1). The computed distortion indices consistently overpredict the distortion due to the overestimate of the total pressure loss in the counter-rotating vortex pair (Table 3). Nonetheless, the close agreement between the computed and experimental surface pressure

**Table 3   Total pressure distortion indices for baseline geometry**

| Parameters | Value | | | | |
|---|---|---|---|---|---|
| | $p_0/p_{0,\text{ref}}$ | $DC(45°)$ | $DC(90°)$ | $DC(135°)$ | $DC(180°)$ |
| Experiment | 0.9655 | 0.559 | 0.370 | 0.303 | 0.181 |
| Baseline computation | 0.9680 | 0.700 | 0.622 | 0.504 | 0.261 |
| | $p_0/p_{0,\text{ref}}$ | $DC(60°)$ | $DC(90°)$ | $DC(120°)$ | |
| Experiment | 0.9671 | 0.4155 | 0.3572 | 0.2891 | |
| Baseline computation | 0.9680 | 0.686 | 0.622 | 0.564 | |

(Figs. 2–7) lends credance to the computation and its subsequent use for reducing the distortion at the outflow.

## Optimization Design

### Geometry Modification

From the baseline computation, we are able to identify the starting point of the separation on the plane of symmetry at $s/d = 2$. Downstream of the separation region, the secondary flows become stronger and, thereby, increase the total pressure distortion. Our idea is to try to delay or even eliminate this separation on the lower surface and, hence, to reduce the distortion at the outflow.
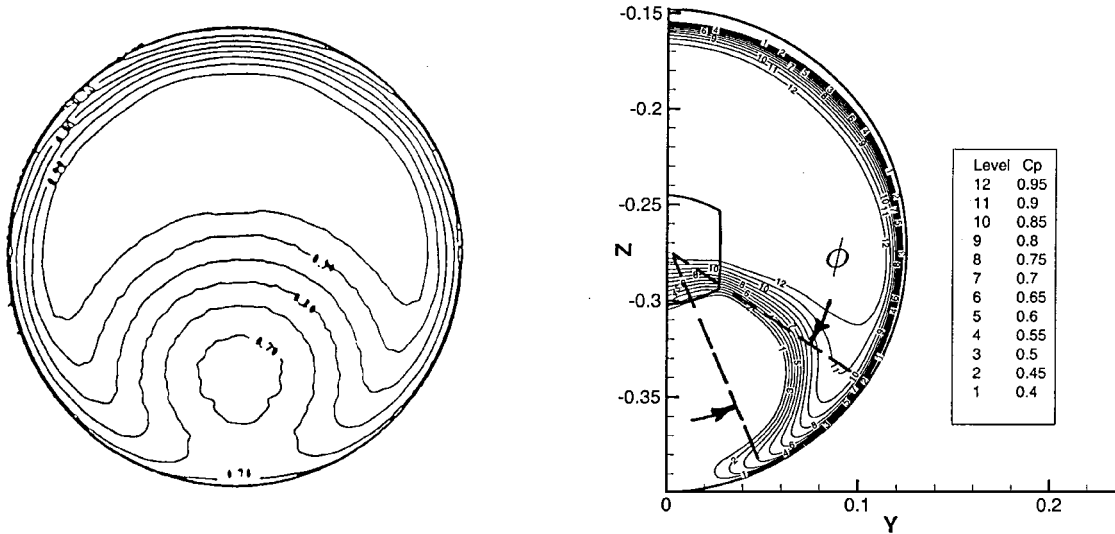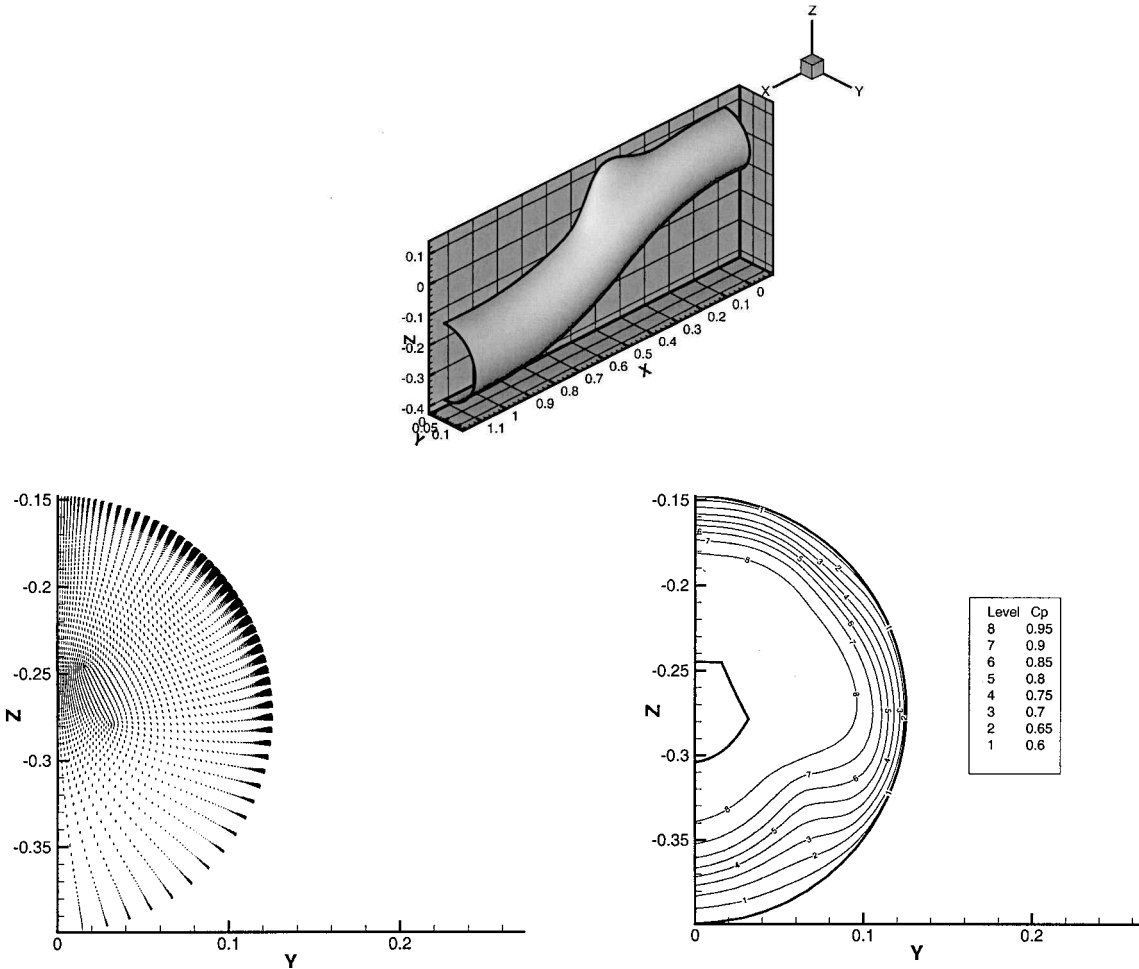


Fig. 10   Total pressure coefficient at plane E.





Fig. 11   Optimal diffuser shape; crossflow velocity and total pressure coefficient at plane E.

**Table 4 Total pressure distortion indices for optimal design**

| Parameters | $p_0/p_{0,\text{ref}}$ | $DC$ (45°) | $DC$ (90°) | $DC$ (135°) | $DC$ (180°) |
|---|---|---|---|---|---|
| | | | Value | | |
| Baseline computation | 0.9680 | 0.700 | 0.622 | 0.504 | 0.2612 |
| Opt. design | 0.9665 | 0.2062 | 0.2047 | 0.1636 | 0.0940 |
| Difference (%) | 0.15 | 70.5 | 67.1 | 67.5 | 64.0 |
| | $p_0/p_{0,\text{ref}}$ | $DC$ (60°) | $DC$ (90°) | $DC$ (120°) | |
| Baseline computation | 0.9680 | 0.6866 | 0.622 | 0.505 | |
| Opt. design | 0.9665 | 0.1997 | 0.2047 | 0.1845 | |
| Difference (%) | 0.15 | 70.9 | 67.1 | 63.5 | |

Two design variables $\alpha$ and $\beta$ are specified. These two design variables give the perturbation of the surface control points that, therefore, modify the surface geometry and corresponding flowfield. The perturbation to the control points is assumed to be Gaussian

$$\Delta = \alpha \exp\left\{-[(s - s_0)/\beta]^2\right\} \qquad (32)$$

where $\alpha$ and $\beta$ are the height and width of the perturbation and $s$ is the centerline curve length. The location of the center of the perturbation is taken to be $s_0 = 0.4084$ m, which corresponds to the experimental separation point on the lower centerline plane (Table 2). The choice is based on the assumption that the perturbation would need to affect the flow in the vicinity of the separation in the baseline geometry to reduce the distortion at the outflow. This perturbation is only applied to the control points that are located on the $y = 0$ plane and above the diffuser to maintain symmetry. From Eq. (32), it is evident that the perturbation vanishes for $|s - s_0| \gg \beta$, thereby limiting the perturbation effect.

### Optimization

We performed an automated optimization of the subsonic diffuser design. Two design variables $\alpha$ and $\beta$, which are defined in Eq. (32), are employed. The configuration of the design variables in the design case is $0.0 \leq \alpha \leq 0.15315$ m and $0.0983 \leq \beta \leq 0.15135$ m. The objective of the optimization is to reduce the distortion indices $DC(\phi)$. Based on a trade study,[27] we concluded that all of the distortion indices behave similarly. Thus, it suffices to consider one distortion index for example, $DC$ 45 deg, for the objective function. The automated optimization required six iterations.

The optimal results are indicated in Fig. 11 and Table 4. The diffuser shape is characterized by a large bump on the upper surface that creates a separated flow region on the upper surface. This effectively reduces the crossflow and, thereby, reduces the distortion at the outflow by 63–71%. The crossflow velocity vectors at plane E show a general motion toward the upper surface, in contrast to the baseline geometry wherein the crossflow was strongly toward the lower surface at plane E. This yields a more axisymmetric total pressure distribution at plane E, as indicated in Fig. 11. The mean total pressure recovery remains essentially unchanged because the separated region generated by the bump is essentially a closed bubble and, consequently, does not introduce low energy fluid into the duct flow.

### Conclusions

An automated design of a three-dimensional subsonic diffuser has been achieved. The objective of the optimization is to reduce total pressure distortion while maintaining the same total pressure recovery. Computations of the baseline geometry were performed including a grid refinement study. The computational results were compared with the experiment and the computation of Harloff et al.[8,9] The computed surface pressure distributions are in good agreement with the experimental data and are more accurate than those of Harloff et al. The computed total pressure distortion indices, measured at the downstream station, overpredict the experiment due to an overestimate in the total pressure loss inside the counter-rotating vortex pair. The computation accurately predicts the location of

separation on the lower centerline plane. An automated optimal design of the diffuser was performed using two design variables that changed the shape of the upper surface of the diffuser at the approximate axial location of the flow separation in the baseline configuration. The shape change is a bump that causes a local separated zone on the upper surface. This separated zone generally reverses the direction of the crossflow velocity, and, hence, the total pressure distortion at the outflow is reduced. Typical reduction in total pressure distortion is 70%. The mean total pressure at the outflow is essentially unchanged. This study demonstrates the capability to reduce total pressure distortion by modification of the surface shape of the diffuser.

Several additional factors need to be considered in future research for practical application of the results obtained in this study. These include 1) the effect of the bump on the diffuser structural behavior, 2) the effect of inlet angle of attack and/or sideslip, that is, asymmetric inflow boundary layer, on the flow distortion in the presence of a bump, and 3) unsteady effects associated with engine surge, inlet dynamic maneuver, or the separation region introduced by the bump (all of which would require modification of the constant pressure outflow boundary condition).

### References

[1]Weske, J. R., "Pressure Loss in Ducts with Compound Elbows," NACA Wartime Rept., 1943.

[2]Henry, J. R., "Design of Power-Plant Installations Pressure-Loss Characteristics of Duct Components," NACA Wartime Rept. WC-39, 1943.

[3]Bansod, P., and Bradshaw, P., "The Flow in S-shaped Ducts," *Aeronautical Quarterly*, Vol. 23, No. 2, 1972, pp. 131–140.

[4]Guo, R. W., and Seddon, J., "An Investigation of the Swirl in an S-Duct," *Aeronautical Quarterly*, Vol. 34, No. 2, 1983, pp. 99–129.

[5]Wellborn, S. R., Reichert, B. A., and Okiishi, T. H., "An Experimental Investigation of the Flow in a Diffusing S-Duct," AIAA Paper 92-3622, July 1992.

[6]Abdallah, S., and Hamed, A., "Inviscid Solution for the Secondary Flow in Curved Ducts," *AIAA Journal*, Vol. 19, No. 8, 1981, pp. 993–999.

[7]Smith, C. F., Bruns, J. E., Harloff, G. J., and DeBonis, J. R., "Three-Dimensional Compressible Turbulent Computations for a Diffusing S-Duct," NASA CR 4392, 1991.

[8]Harloff, G. J., Reichert, B. A., and Sirbaugh, J. R., "Navier–Stokes Analysis and Experimental Data Comparison of Compressible Flow Within Ducts," NASA TM 105796, 1992.

[9]Harloff, G. J., Reichert, B. A., and Wellborn, S. R., "Navier–Stokes Analysis and Experimental Data Comparison of Compressible Flow in a Diffusing S-Duct," AIAA Paper 92-2699, June 1992.

[10]Hah, C., "Calculation of Various Diffuser Flows with Inlet Swirl and Inlet Distortion Effects," *AIAA Journal*, Vol. 21, No. 8, 1983, pp. 1127–1133.

[11]Harloff, G. J., DeBonis, J. R., Smith, C. F., and Bruns, J. E., "Three-Dimensional Turbulent Computations for a Nondiffusing S-Duct," NASA CR 4391, 1991.

[12]Demuren, A. O., "Calculation of Turbulence-Driven Secondary Motion in Ducts with Arbitrary Cross Section," *AIAA Journal*, Vol. 29, No. 4, 1991, pp. 531–537.

[13]Pao, S. P., Carlson, J. R., and Abdul-Hamid, K. S., "Computational Investigation of Circular-to-Rectangular Transition Ducts," *Journal of Propulsion and Power*, Vol. 10, No. 1, 1994, pp. 95–100.

[14]Gerlach, C. R., and Schroeder, E. C., "Study of Minimum Pressure Loss in High Velocity Duct Systems," NASA Interim TR, 1969.

[15]Weng, P. F., and Guo, R. W., "New Method of Swirl Control in a Diffusing S-Duct," *AIAA Journal*, Vol. 30, No. 7, 1992, pp. 1918, 1919.

[16]Vakili, A. D., Wu, J. M., and Bhat, M. K., "Experimental Investigation of Secondary Flows in a Diffusing S-Duct," Univ. of Tennessee Space Inst. TR UTSI 86/14, Nashville, TN, 1986.

[17]Lin, P., and Jules, K., "Optimized Multidisciplinary System Design for Aircraft and Propulsion Systems," AIAA Paper 98-3265, June 1998.

[18]Taylor, H. D., "Retractable Vortex Generators," United Aircraft Corp. Research Dept. Rept. M-15355-3, 1950.

[19] Brown, A. C., Nawrocki, H., and Paley, P., "Subsonic Diffusers Designed Integrally with Vortex Generators," *Journal of Aircraft*, Vol. 5, No. 3, 1968, pp. 221–229.

[20] Mitchell, G. A., and Davis, R. W., "Performance of Centerbody Vortex Generators in an Axisymmetric Mixed Compression Inlet at Mach Numbers from 2.0 to 3.0," NASA TN D-4675, 1968.

[21] Reichert, B. A., and Wendt, B. J., "Improving Curved Subsonic Diffuser Performance with Vortex Generators," *AIAA Journal*, Vol. 34, No. 1, 1996, pp. 65–72.

[22] Anderson, B. H., and Gibb, J., "Study on Vortex Generator Flow Control for the Management of Inlet Distortion," *Journal of Propulsion and Power*, Vol. 9, No. 3, 1993, pp. 422–430.

[23] Mayer, D. W., Anderson, B., and Johnson, T., "3D Subsonic Diffuser Design and Analysis," AIAA Paper 98-3418, July 1998.

[24] Reddy, E. S., and Reddy, D. R., "Aerodynamic Shape Optimization of A Subsonic Inlet Using 3-D Euler Computation," AIAA Paper 95-2757, July 1995.

[25] Burgreen, G. W., Baysal, O., and Eleshaky, M. E., "Improving the Efficiency of Aerodynamic Shape Optimization," *AIAA Journal*, Vol. 32, No. 1, 1994, pp. 69–76.

[26] Porro, A. R., Hingst, W. R., Wasserbauer, C. A., and Andrews, T. B., "The NASA Lewis Research Center Internal Fluid Mechanics Facility," NASA TM 105187, 1991.

[27] Zhang, W.-L., "Three-Dimensional Subsonic Diffuser Design Optimization and Analysis," Ph.D Dissertation, Dept. of Mechanical and Aeronautic Engineering, Rutgers Univ., New Brunswick, NJ, May 1999.

[28] White, F. M., *Viscous Fluid Flow*, McGraw–Hill, New York, 1991.

[29] Baldwin, B. S., and Lomax, H., "Thin Layer Approximation and Algebraic Model for Separated Turbulent Flows," AIAA Paper 78-257, Jan. 1978.

[30] Degani, D., Schiff, L., and Levy, Y., "Physical Considerations Governing Computation of Turbulent Flows over Bodies at Large Incidence," AIAA Paper 90-0096, Jan. 1990.

[31] "General Aerodynamic Simulation Program," Aerosoft, Inc., Blacksburg, VA, 1996.

[32] York, B. J., "Evaluation of the Baldwin–Lomax Turbulence Model for a Class of Boundary Layer Flows," M.S. Thesis, Dept. of Mechanical and Aeronautic Engineering, Rutgers Univ., New Brunswick, NJ, Oct. 1984.

[33] "GridPro/az3000 User's Guide and Reference Manual," Program Development Corp., White Plain, NY, 1996.

[34] Van Leer, B., Tai, C.-H., and Powell, K. G., "Design of Optimally Smoothing Multi-Stage Schemes for the Euler Equations," AIAA Paper 89-1933, Jan. 1989.

[35] Lawrence, C., Zhou, J. L., and Tits, A. L., "User's Guide for CFSQP, A Code for Solving Constrained Nonlinear Optimization Problem, Generating Iterates Satisfying All Inequality Constraints," Electrical Engineering Dept., TR-94-16rl, Univ. of Maryland, College Park, MD, 1996.

[36] Mayne, D. Q., and Polak, E., "Feasible Directions Algorithms for Optimization Problems with Equality and Inequality Constraints," *Math. Programming*, Vol. 11, 1976, pp. 67–80.

[37] Panier, E. R., and Tits, A. L., "On Combining Feasibility, Descent and Superlinear Convergence in Inequality Constrained Optimization," *Math. Programming*, Vol. 59, No. 2, 1993, pp. 261–276.

[38] Bonnans, J. F., and Panier, E. R., "Avoiding the Maratos Effects by Means of a Nonmontone Line Search, Inequality Constrained Problems-Feasible Iterates," *SIAM Journal on Numerical Analysis*, Vol. 29, No. 4, 1992, pp. 1187–1202.

[39] Zhou, J. L., and Tits, A. L., "Nonmonotone Line Search for Minimax Problems," *Journal of Optimization Theory and Applications*, Vol. 76, No. 3, 1993, pp. 455–476.

[40] Zhang, W.-L., and Knight, D. D., "Automatic Design and Analysis of Three Dimensional Subsonic Diffuser," AIAA Paper 2000-0665, Jan. 2000.

[41] Tobak, M., and Peake, D., "Topology of Three-Dimensional Separated Flows," *Annual Review of Fluid Mechanics*, 1982, Vol. 14, pp. 61–85.